Can statistics of turbulent tracer dispersion be inferred from camera observations of SO_2 in the ultraviolet? A modelling study

Arve Kylling[1], Hamidreza Ardeshiri[2], Massimo Cassiani[1], Anna Solvejg Dinger[3], Soon-Young Park[4], Ignacio Pisso[1], Norbert Schmidbauer[1], Kerstin Stebel[1], and Andreas Stohl[5]

[1]NILU - Norwegian Institute for Air Research, NO-2007 Kjeller, Norway
[2]GexCon AS, Bergen, Norway
[3]PGS, Oslo, Norway
[4]Center for Earth and Environmental Modeling Studies, Gwangju Institute of Science and Technology, Gwangju, Republic of Korea
[5]Department of Meteorology and Geophysics, University of Vienna, Vienna, Austria

Correspondence to: Arve Kylling (arve.kylling@nilu.no)

Abstract. Atmospheric turbulence and in particular its effect on tracer dispersion may be measured by cameras sensitive to the absorption of ultraviolet (UV) sun-light by sulfur dioxide (SO_2), a gas that can be considered a passive tracer over short transport distances. We present a method to simulate UV camera measurements of SO_2 with a 3D Monte Carlo radiative transfer model which takes input from a large eddy simulation (LES) of a SO_2 plume released from a point source. From the simulated images the apparent absorbance and various plume density statistics (centerline position, meandering, absolute and relative dispersion, and skewness) were calculated. These were compared with corresponding quantities obtained directly from the LES. Mean differences of centerline position, absolute and relative dispersions, and skewness between the simulated images and the LES were generally found to be smaller than or about the voxel resolution of the LES. Furthermore sensitivity studies were made to quantify how changes in solar azimuth and zenith angles, aerosol loading (background and in plume), and surface albedo impact the UV camera image plume statistics. Changing the values of these parameters within realistic limits have negligible effect on the centerline position, meandering, absolute and relative dispersions, and skewness of the SO_2 plume. Thus, we demonstrate that UV camera images of SO_2 plumes may be used to derive plume statistics of relevance for the study of atmospheric turbulent dispersion.

1 Introduction

Air motion in the lowest part of the atmosphere is over land bounded by a solid surface of varying temperature and roughness. This part of the atmosphere is named the planetary boundary layer (PBL, Stull, 1988). It responds quickly to surface radiation changes, and the air motion in the PBL is nearly always turbulent. A substance released into this turbulent atmosphere will, at locations downwind of its source, experience concentration fluctuations that are important, particularly if responses are non-linear; for example with respect to toxicity, flammability and odour detection (e.g. Hilderman et al., 1999; Schauberger et al., 2012; Gant and Kelsey, 2012) and non-linear chemical reactions (Brown and Bilger, 1996; Vilà-Guerau de Arellano et al., 2004; Cassiani et al., 2013). The COMTESSA project (Camera Observation and Modelling of 4D Tracer Dispersion in the

Atmosphere; https://comtessa-turbulence.net/) aims to "elevate the theory and simulation of turbulent tracer dispersion in the atmosphere to a new level by performing completely novel high-resolution 4D measurements". Over short transport distances, sulfur dioxide (SO_2) may be considered to be a passive tracer. Furthermore, SO_2 strongly absorbs radiation in part of the UV spectrum and may thus be detected by for example UV sensitive cameras (see for example Kern et al., 2010b, and references therein). Within COMTESSA, six UV cameras have been built to measure SO_2 densities from various viewing directions. A series of experiments with puff and continuous releases of SO_2 from a tower have been performed as described by Dinger et al. (2018). It is known from measurements of volcanic SO_2 emissions that aerosol and viewing geometry affect the retrieved SO_2 amounts (Kern et al., 2013). Furthermore, variations in surface albedo and solar zenith and azimuth angles may have an impact. The influence of these factors on the UV camera images, the deduced SO_2 amounts and density statistics needs to be quantified and, if necessary, corrected for.

Kern et al. (2013) performed radiative transfer simulations including a circular SO_2 plume, to estimate the effect of plume distance, SO_2 amount, and aerosol on the radiance at a UV camera location. However, to the authors knowledge, UV camera images have not been simulated before. We present a novel method to simulate UV camera images of a dispersing SO_2 plume using a 3D radiative transfer model. The 3D descripton of the SO_2 plume is provided by large eddy simulation (LES) and are used in lieu of real atmospheric flow. The simulated images are used to examine how various factors (solar angles, aerosol content, and surface albedo) affect the statistical parameters characterizing the SO_2 plume dispersion. The large eddy simulation (LES) providing the input to the radiative transfer modelling, the radiative transfer model used to simulate the camera images and the statistical parameters are described in section 2. The effects of solar azimuth and zenith angles, surface albedo, background aerosol, and aerosols in the plume on plume density statistics are presented in section 3. Furthermore, the plume density statistics from the simulated images are compared with statistics derived directly from the LES simulations. The paper ends with the conclusions in section 4.

2 Methods

2.1 Large eddy simulation (LES)

Large eddy simulation is nowadays viewed as a popular tool in many applied atmospheric dispersion studies, especially of the urban environment and for critical applications such as the release of toxic gas substances (e.g. Fossum et al., 2012; Lateb et al., 2016). LES provides access to the three dimensional turbulent flow field and it is sometimes used as a replacement for experimental measurements at high Reynolds numbers. In this methodology, the large scales of the turbulent flow are explicitly simulated while a low-pass filter is applied to the governing equations to remove the small scales information from the numerical solution. The effects of the small scales are then parameterized by means of a sub-grid scale (SGS) model (e.g. Deardorff, 1973; Moeng, 1984; Pope, 2000; Celik et al., 2009). We used the Parallelized Large-Eddy Simulation Model (PALM, Raasch and Schröter, 2001; Maronga et al., 2015) to solve the filtered, incompressible Navier-Stokes equations in Boussinesq-approximated form, at infinite Reynolds number. A three dimensional domain of 1000 m $\times$ 375 m $\times$ 250 m in the along wind (x), crosswind (y) and vertical (z) directions respectively, was simulated with a grid resolution of $nx \times ny \times nz =$

$1024 \times 384 \times 256$. Here nx, ny, nz are the number of grid nodes in along wind, crosswind and vertical directions, respectively. This implies that the size of a grid cell is $0.98^3\,\mathrm{m}^3 \approx 1\,\mathrm{m}^3$. The release point was located at 25 and 150 m above the ground, depending on camera view direction, see section 2.2.

The neutral boundary layer was simulated as an incompressible half channel flow at an infinite Reynolds number. The flow was driven by a constant pressure gradient. For the velocity, periodic boundary conditions were used on the lateral boundaries while on the top, strictly symmetric, stress free, condition was applied. The bottom wall was not explicitly resolved but a constant flux layer was used as is commonly done in atmospheric simulations. Non-periodic boundary conditions were set for the passive scalar. For further information on the model set-up see also Ardeshiri et al. (2020).

The LES calculates 3D SO_2 concentrations as a function of time. The SO_2 concentrations are used as input to the 3D radiative transfer model simulations. A total of 100 time frames were calculated with a time resolution of 6.25 s. For the sensitivity studies one randomly chosen time frame was used, while seven and nine randomly chosen frames were used for the reference case calculation (see section 3). Both parts of the plume close to the release point and further downstream were used as input for the camera simulations. In Fig. 1 examples are provided of the part of the plume viewed by the different cameras (see section 2.2 for camera definition). Figs. 1a and 1b show the SO_2 column densities along the y and z-axes, respectively, for one instant of the LES simulation. Fig. 1a shows approximately the part of the plume seen by camera A Figs. 1c and 1d show the part of the plume viewed by cameras B and C, respectively.

2.2 Radiative transfer simulations

The UV camera images were simulated with the 3D MYSTIC Monte Carlo radiative transfer model which was run within the libRadtran framework (Mayer et al., 2010; Emde et al., 2010; Buras and Mayer, 2011; Mayer and Kylling, 2005; Emde et al., 2016). MYSTIC includes an option to calculate the radiation impinging on a camera with a prescribed number of pixels in a plane defined by the location of the camera within a 3D domain and the camera viewing direction. For this option the MYSTIC Monte Carlo model is run in backward mode. The MYSTIC camera simulation capabilities have earlier been used by for example Kylling et al. (2013) to simulate infrared satellite images. Here it is used to simulate radiative transfer to a UV camera at wavelengths suitable for the detection of SO_2. Thus, for each camera pixel, spectra were calculated for wavelengths ranging between 300 and 350.5 nm. The spectral resolution was 0.1 nm in order to capture the fine structure of the SO_2 cross section. The spectra were weighted with spectral response functions (about 10 nm width) representing cameras with mounted on-band (sensitive to SO_2 absorption, centred at 310 nm) and off-band (barely sensitive to SO_2 absorption, centred about 330 nm) filters similar to those described by Gliß et al. (2018). Quantum efficiency of the detector and geometrical effects related to lens/camera optics were not included in the camera simulations. SO_2 plume concentrations were adopted from the LES simulations described in section 2.1 and the spectrally dependent SO_2 absorption cross section was taken from Hermans et al. (2009).

A finite 3D domain (bird's eye view provided in Fig. 2) is defined for the radiative transfer simulations. The SO_2 plume is embedded in this domain and is viewed from the side at a distance of about 250 m by the UV camera, which is placed 1 m

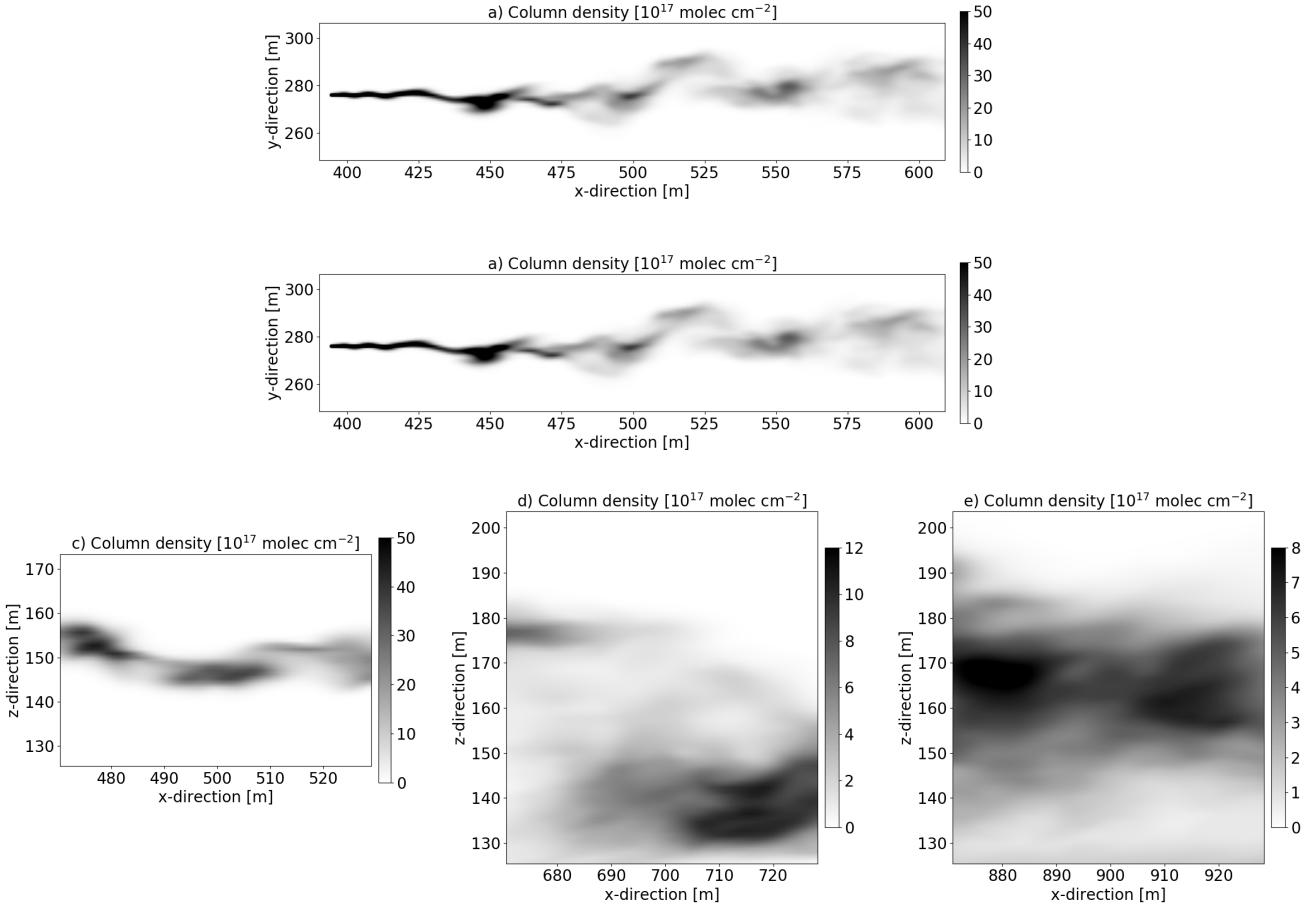

Figure 1. a) SO_2 column densities from the LES (time frame no. 2) integrated along the vertical z-direction. This corresponds to the part of the plume viewed by camera A. b) Corresponding SO_2 column densities integrated along the cross-wind y-direction. c-e) LES SO_2 column densities (time frames no. 61, 10 and 91) integrated along the cross-wind y-direction, corresponding to the part of the plume viewed by cameras B, C and D respectively. Note the different scales of the grayscale bars.

above the surface. This camera-plume distance is comparable to that used during part of the first COMTESSA field campaign described by Dinger et al. (2018).

Four different cameras at different locations and viewing geometries were simulated. These are summarized in Table 1. Camera A captures the plume from its release point and about 200 m downwind. It sees the plume released at an altitude of 25 m and thus have a low angle viewing elevation, see Table 1. Cameras B, C and D resembles a different experimental situtation with the plume release altitude of 150 m. These cameras thus have a larger viewing elevation. Camera A is placed at the same x-direction location as camera A, but as a smaller horizontal FOV to focus on the more mature parts of the plume.

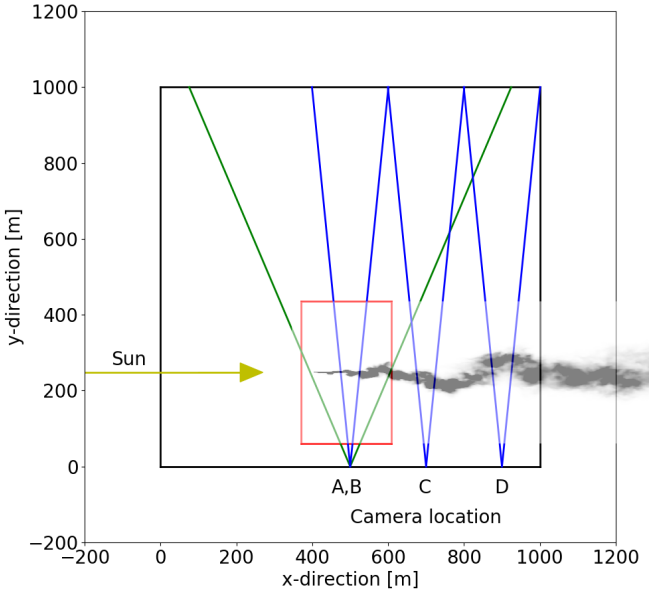

Figure 2. Bird's eyes view of the 3D domain (black square) and the SO_2 plume location within the domain (red square for camera A simulation, shifted along x-axis for the other cameras). The UV cameras are located where the two green or blue lines intersect. The lines indicate the horizontal field-of-view of the cameras whose location is given in Table 1. The column density (similar to the upper plot in Fig. 1) of the plume is included for illustrative purpose. The direction of the incoming Sun ray is shown by the yellow line.

Table 1. Location and geometric specification of the three simulated cameras. All cameras were placed 1 meter above the surface.

Camera	FOV (degrees)	Viewing elevation (degrees)	No. of pixels. (horizontal×vertical)	x-location (m)
A	46°×10°	5.73°	400×88	500
B	11.5°×30°	30.7°	100×264	500
C	11.5°×30°	30.7°	100×264	700
D	11.5°×30°	30.7°	100×264	900

Cameras C and D are placed further downwind and views the plume about 300 and 500 m downwind from the release point, respectively.

The LES voxel resolution is about 1 m^3 which at a distance of 250 m corresponds to 0.004 rad=0.23°. To ensure sufficient spatial sampling the camera resolution was specified to be about half the LES voxel resolution. To be able to see the plume at the various camera position the camera field of view (FOV) was varied and the number of pixels adopted to give a camera

resolution of about 0.5 m at the plume. It is noted that the UV cameras used by Dinger et al. (2018) had 1392×1040 pixels. The reason and justification for using fewer pixels in the simulated camera are twofold: 1) With the simulated camera it is possible to zoom onto the plume as one always knows where the plume is. In an experimental setting, the plume usually covers only part of the FOV, to allow for changes in wind direction and, thus, changes in plume position; 2) The computer time and memory requirements increase as the number of pixels increases. It is thus advantageous to use as few pixels as needed to cover the plume.

As the COMTESSA field campaigns are being carried out primarily in central Norway during the summer time, solar zenith angles of 40° and 60° were considered. When not otherwise noted (see section 3.2), the sun was assumed to be perpendicular to the camera viewing direction, see Fig. 2.

To further save computer memory and time, a full 3D description of the plume is given only in the part of the domain containing the plume seen by the camera (red square in Fig. 2). Outside the red square, the plume is not included. Energy conservation is ensured by using periodic boundary conditions, that is, photons leaving the domain on one side enter the domain again on the opposite side. Not having perodic boundary conditions would let the photons leave the domain and thus not being accounted for. Periodic boundary conditions imply that effectively the plume within the domain keeps on repeating itself in the horizontal. Thus the plume may be seen several times by the camera if not care is taken when setting up the geometry of the computational domain, the location of the plume within the domain, and the camera. However, sometime these "ghost" plumes are unavoidable due to the geometry and computational resources. It is noted that the "ghost" plumes get smaller and smaller in the camera view the further away they are from the domain with the camera. For camera A "ghost" plumes pose a challenge due to the low altitude plume and camera viewing angles close to the horizon. Great care was thus taken when setting the domain size and the camera A field of view to avoid "ghost" plumes in the simulated images. Still, part of a secondary "ghost" plume is present in some of the images. These "ghost" plumes have been removed from the analysis presented below for camera A.

For representing the ambient atmosphere the mid-latitude summer atmosphere of Anderson et al. (1986) was used. The surface albedo is small in the UV for non-snow covered surfaces and was thus set to zero when not otherwise noted (see section 3.4). Aerosols were included for specific sensitivity tests that are described in section 3.3.

The radiative transfer simulations were run on a Linux cluster utilizing 10 processors in parallel with each process needing about 10-15 GB of memory depending on whether aerosols in the plume were included or not. The MYSTIC Monte Carlo radiative transfer simulation is statistical in nature and the simulated images thus contain statistical noise. To achieve a noise level of about the same order of magnitude as the measurements ($\approx 1\%$), a sufficient number of photons needs to be traced. For each pixel and wavelength 2000 photons were traced. This gave simulation times for one on- and one off-band image of about 120-140 hours, and ensured that for the simulations without aerosol and zero surface albedo at least 93.0% of the pixels had radiances with a relative standard deviation $<1.0\%$. For simulations with background aerosols the corresponding number is 83%.

2.3 Analysis methodology

The apparent absorbance for the on-band camera is given by Mori and Burton (2006) and Lübcke et al. (2013)

$$\tau_{on} = -\ln \frac{I_{on,M}}{I_{on,0}} \tag{1}$$

Here, $I_{on,M}$ is the on-band radiance and $I_{on,0}$ the background radiance without the SO_2 plume. In addition to absorption by SO_2, τ_{on} may include absorption due to aerosol and plume condensation. Assuming that the absorption by these other constituents varies little with wavelength between the on- and off-band cameras, the extra absorption may be removed by subtracting the off-band absorption:

$$\tau = \tau_{on} - \tau_{off} = -\ln \frac{I_{on,M}}{I_{on,0}} + \ln \frac{I_{off,M}}{I_{off,0}} = \ln \left(\frac{I_{off,M}}{I_{on,M}} \frac{I_{on,0}}{I_{off,0}} \right), \tag{2}$$

where $I_{off,M}$ and $I_{off,0}$ are the off-band radiance and the off-band background radiance respectively. The background images were calculated similar to the plume images, but with the SO_2 concentration set to zero. Below, plume statistics are presented for both τ_{on} and τ.

Ideally, plume statistics from the LES SO_2 concentrations and image derived SO_2 concentrations should be compared. However, for the images this would require simulating a geometry suitable for tomography and tomographic reconstruction of the plume. The slant column density (SCD) is the concentration of a gas along the light path (typically in units of m^{-2}). It is calculated from the LES SO_2 concentrations by tracing individual rays corresponding to individual camera pixels. From apparent absorbances the SCD may be retrieved. For SO_2 camera measurement this is done by calibrating the camera with SO_2 cells and/or concurrent differential optical absorption spectroscopy (DOAS) measurements. The calibration gives a linear relationship between the apparent absorbance and the SCD (see for example Lübcke et al., 2013). Such calibration procedures could be simulated and used to calibrate the simulated images. However, higher order moments (first order moment and upwards) would be the same for the SCD and the apparent absorbance due to the linear relationship between the two. Thus, below we will compare SO_2 SCD from the LES with apparent absorbance from the images. We note that this comparison will not include the zeroth moment (total mass) and that systematic biases may go undetected. While a comparison of the total mass certainly is of interest, this would require a systematic investigation of SO_2 calibration using simulated images, which is beyond the scope of this work.

2.3.1 Plume statistics

For projected LES simulations and the simulated images, the vertical (in the images) plume centerline position, meandering, absolute and relative dispersions, and the skewness were calculated (see e.g. Dosio and de Arellano, 2006). However, the absolute dispersion can only be properly defined using an ensemble or time average. As this is not possible here due to the above mentioned computing limitations, we use the center of the source ($\overline{z} = z_0$) as the reference vertical position.

Each pixel in the camera images and each projection from the LES simulations describe the integrated column amount (ρ_L) of the trace gas along the line of sight (dL):

$$\rho_L = \int \rho dL \tag{3}$$

where ρ is the density of the trace gas. The instantaneous vertical plume centerline position z_m is given by

$$z_m(x) = \frac{\int z \rho_L dz}{\int \rho_L dz} \tag{4}$$

where x and z are the horizontal and vertical positions of the pixel, respectively.

The fluctuations of the absolute, relative and centerline positions are defined as

$$z' = z - z_0 \tag{5}$$

$$z_r = z - z_m \tag{6}$$

$$z'_m = z_m - z_0. \tag{7}$$

It is noted, that with this definition of the absolute position, relative and absolute dispersion are the same at the source location, since meandering here is zero. Also, since we set $\overline{z} = z_0$, there will be correlations between z'_m at different x, which also implies that $\overline{(z'_m)}$ is strictly speaking not a robust reference for defining meandering of the plume. However, the purpose of this study is to investigate the sensitivity of the statistical properties to changes in various atmospheric parameters and this limitation should have minimal impact on the results.

The absolute (σ_z), relative (σ_{zr}) and meandering (σ_{zm}) dispersions are defined as:

$$\sigma_z^2(x) = \frac{\int \rho_L z'^2 dz}{\int \rho_L dz} \tag{8}$$

$$\sigma_{zr}^2(x) = \frac{\int \rho_L z_r^2 dz}{\int \rho_L dz} \tag{9}$$

$$\sigma_{zm}^2 = \frac{\int \rho_L z_m'^2 dx}{\int \rho_L dx} \tag{10}$$

and similarly for the skewnesses:

$$\overline{z'^3} = \frac{1}{\sigma_z^3(x)} \frac{\int \rho_L z'^3 dz}{\int \rho_L dz} \tag{11}$$

$$\overline{z_{zr}'^3} = \frac{1}{\sigma_{zr}^3(x)} \frac{\int \rho_L z_r^3 dz}{\int \rho_L dz} \tag{12}$$

$$\overline{z_{zm}'^3} = \frac{1}{\sigma_{zr}^3(x)} \frac{\int \rho_L z_m'^3 dx}{\int \rho_L dx} \tag{13}$$

These various quantities were calculated both directly from the projected LES simulations and also from the camera images. The former served as a reference ("ground truth") against which the quantities derived from the camera images were compared.

3 Results

We first compare statistical results from the LES and simulated images reference atmospheric conditions. This comparison is made multiple time frames and is done in order to estimate how well the camera derived statistics may reproduce the LES statistics. Next the impact of solar angles, aerosol load, and surface albedo on plume statistics are investigated for a single time frame.

3.1 Reference cases

Figs. 3a and 3b show simulated on- and off-band radiances, respectively, for camera A and the reference case (no aerosol, zero surface albedo and a solar zenith angle of 40°). The strong absorption of SO_2 in the on-band image is clearly visible in

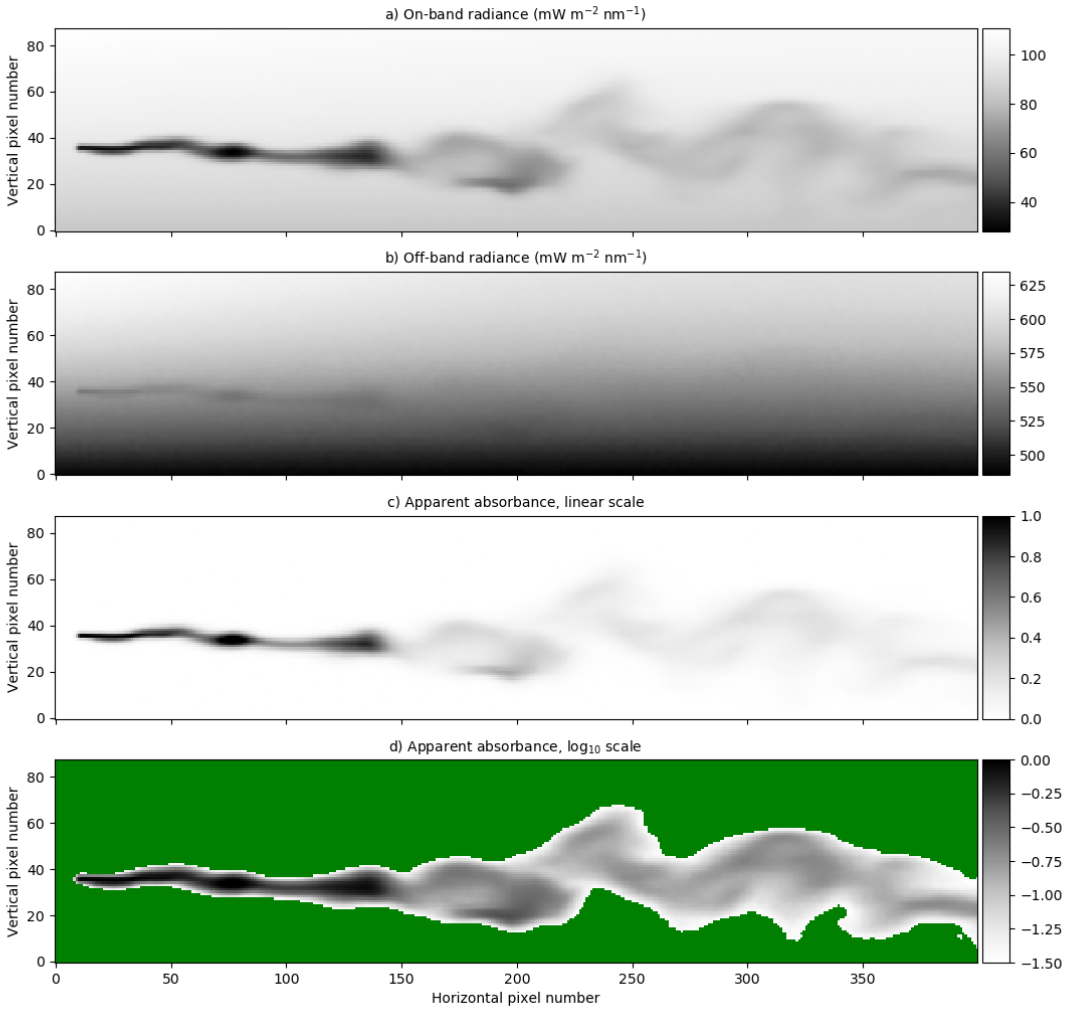

Figure 3. Radiances and apparent absorbance for camera A , same time frame as in Fig. 1. (a) The on-band radiance. (b) The off-band radiance. (c) The apparent absorbance calculated using Eq. 2. (d) Same as (c) but with logarithmic grey scale. The green colour represents pixels for which the apparent absorbance $\tau < 0.03$.

Fig. 3a. There is also a weak SO_2 signal in the off-band image (Fig. 3b). From the on- and off-band images, and corresponding background images not including the SO_2 plume, the apparent absorbance was calculated using Eq. 2. The resulting apparent

absorbance is shown in Fig. 3c on a linear scale and in Fig. 3d on a logarithmic scale. The apparent absorbance is reproduced in Fig. 4a, while Fig. 4b shows the SCD calculated along the line of sights using the LES concentrations. The plume centerline, absolute and relative dispersions, and skewness, as defined in Eqs. 4, 8 and 11, were calculated from the simulated images and the LES images. These are shown as solid lines (LES) and dotted lines (camera simulation) in Figs. 4a and b. Similar plots for cameras B, C and D are presented in Figs. 5-7. Note that the simulated and LES images in Figs. 4-7 differs from those in Fig. 1 due to different viewing directions. In the latter the plumes are viewed at an viewing angle of 0° while for cameras A, B, C and D the viewing angle differs from the horizontal, see Table 1.

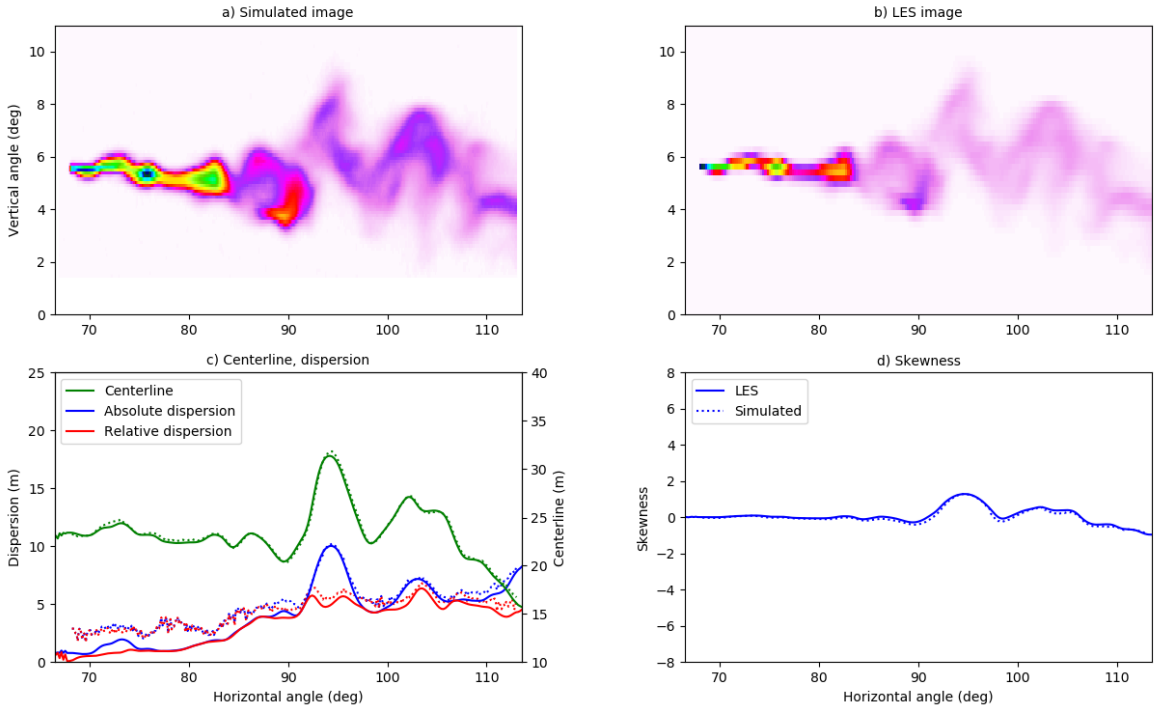

Figure 4. a) The plume apparent absorbance for camera A from Fig. 3c. b) The LES column density integrated along the line of sight. Colorscales in a) and b) are relative and thus no colorbars are provided. c) The centerline, absolute and relative dispersions. d) The skewness.

Overall the behaviour of the centerline, absolute and relative dispersions and skewness calculated from the simulated images is similar to those from the LES densities for all cameras. The centerlines agrees well for all four cameras. For camera A, Fig. 4, the absolute and relative dispersions from the camera are larger than those from the LES for the plume downwind to about 100 m (corresponding to $\approx 90°$ horisontal viewing angle) from the release point. For camera B, Fig. 5, all quantities agree well, while for cameras C (Fig. 6) and D (Fig. 7), the camera dispersions are larger than the LES dispersions by about 50-60% and the magnitude of the skewness from the camera is also larger.

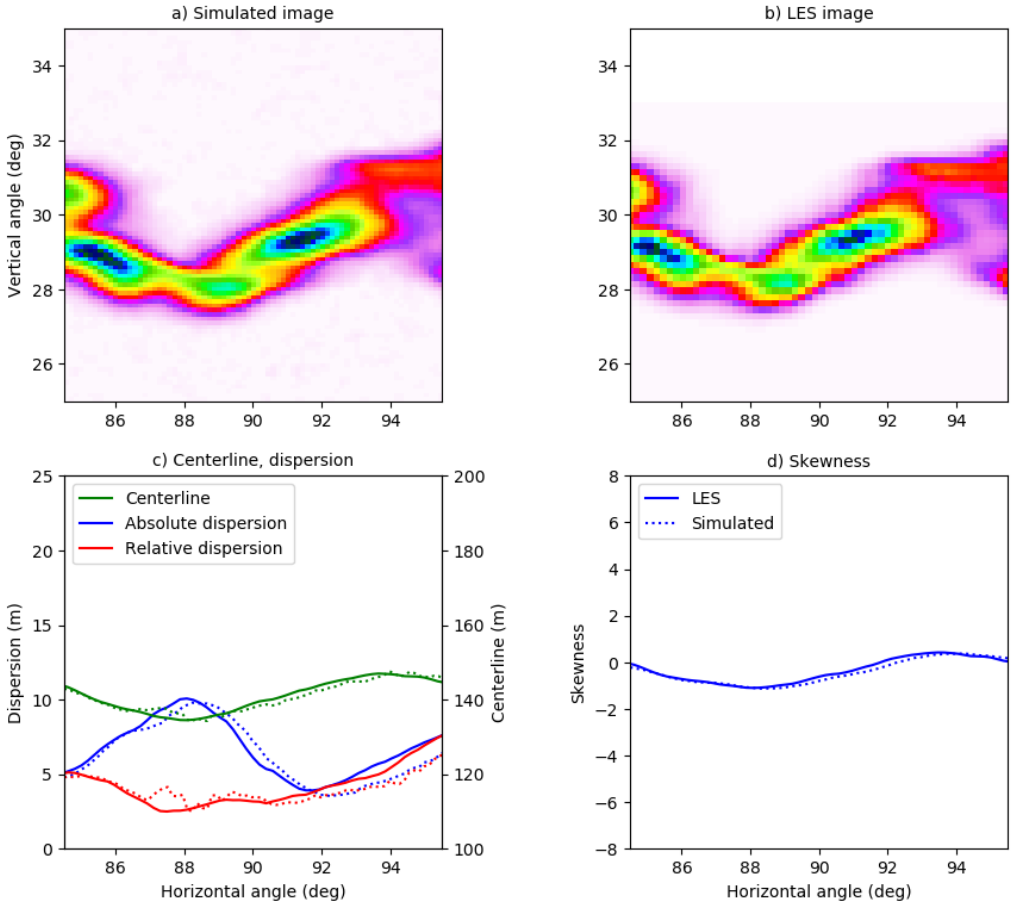

Figure 5. Similar to Fig. 4, but for camera B and time step 61.

To shed further light on the differences between the images from the radiative transfer simulation and the LES we show the probability density function (pdf) of the column densities from the LES and simulated images in Fig. 8. These pdfs represent area sample pdfs and cover the full images. For camera A the pdfs differ for intermediate values, where an artificial secondary peak is created in the pdf for the simulated image. This is most likely due to the diffusive nature of the radiative transfer in the young part of the plume (horizontal angle smaller than about 85°) where the LES plume is of the size a few voxels. However, the SO_2 absorption signal is strong and thus the centerline, dispersions and skewness agree well for the dispersed part of the plume. For camera B the pdfs are similar and this is reflected in the good agreement between the statistical quantities presented in Fig. 5. This indicates that the when the plume is large enough compared to the pixel resolution the camera can capture the plume well . The pdfs for camera C exhibit much the same behaviour. However, at this further downwind location, the plume is more dispersed, the SO_2 absorption signal weaker and sometime beyond detection (thus the lower cut-off in the pdf of the

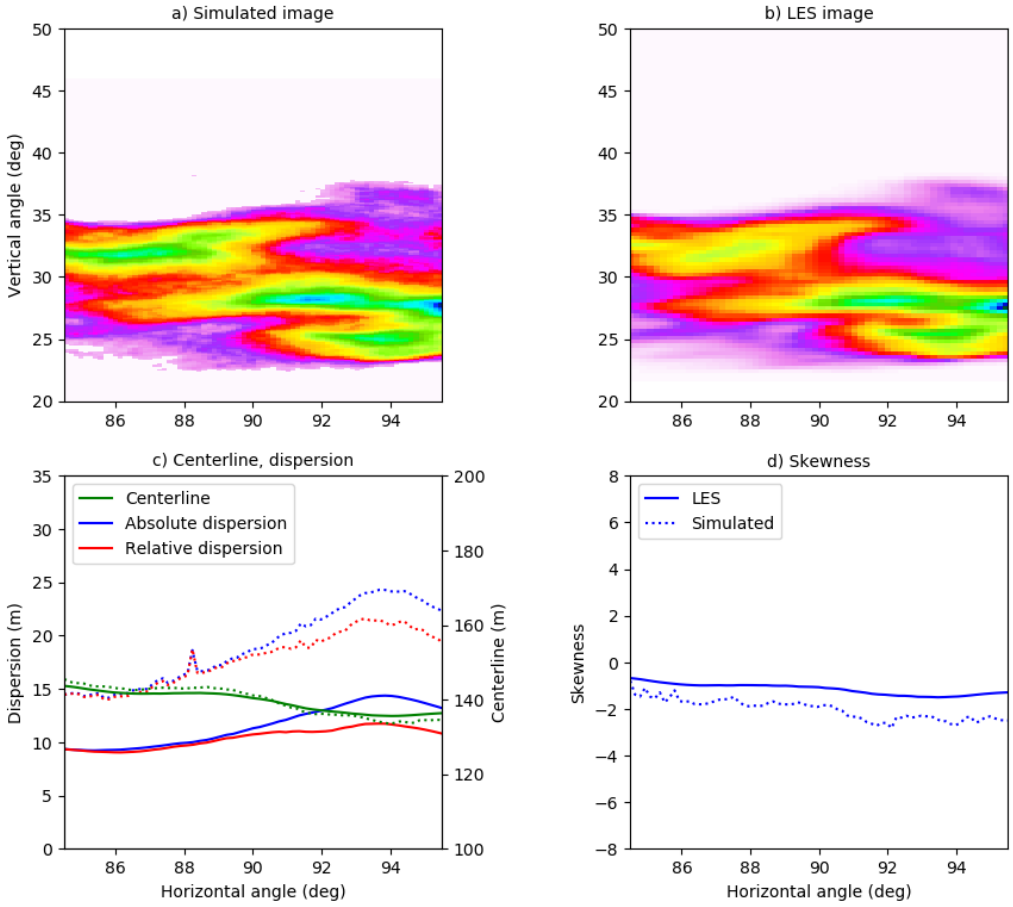

Figure 6. Similar to Fig. 4, but for camera C and time step 10.

simulated image). The weaker absorption signal implies that the statistical noise from the Monte Carlo based radiative transfer simulation becomes discernible and increases the dispersions compared to the LES, Fig. 6. A similar situation is evident for camera D, see pdfs in Fig. 8 and statistical quantities in Fig. 7

As noted above, a large number of images such as in Fig. 3 is required to estimate the parameters of interest for description of turbulence. This is not computationally feasible with available resources. However, it is noted that if the instantaneous statistics are correct, the ensemble statistics will also be correct. This is not necessarily true the other way around. To provide an estimate of the difference between the statistical quantities from the simulated images and the LES densities, the differences between the centerline, the absolute and relative dispersions and the skewness, were calculated for seven (camera A) and nine (cameras B, C and D) random time steps. The mean differences and the standard deviations are summarized in Table 2. The mean differences between the quantities from the simulated images and the LES densities are small for cameras A and B. For

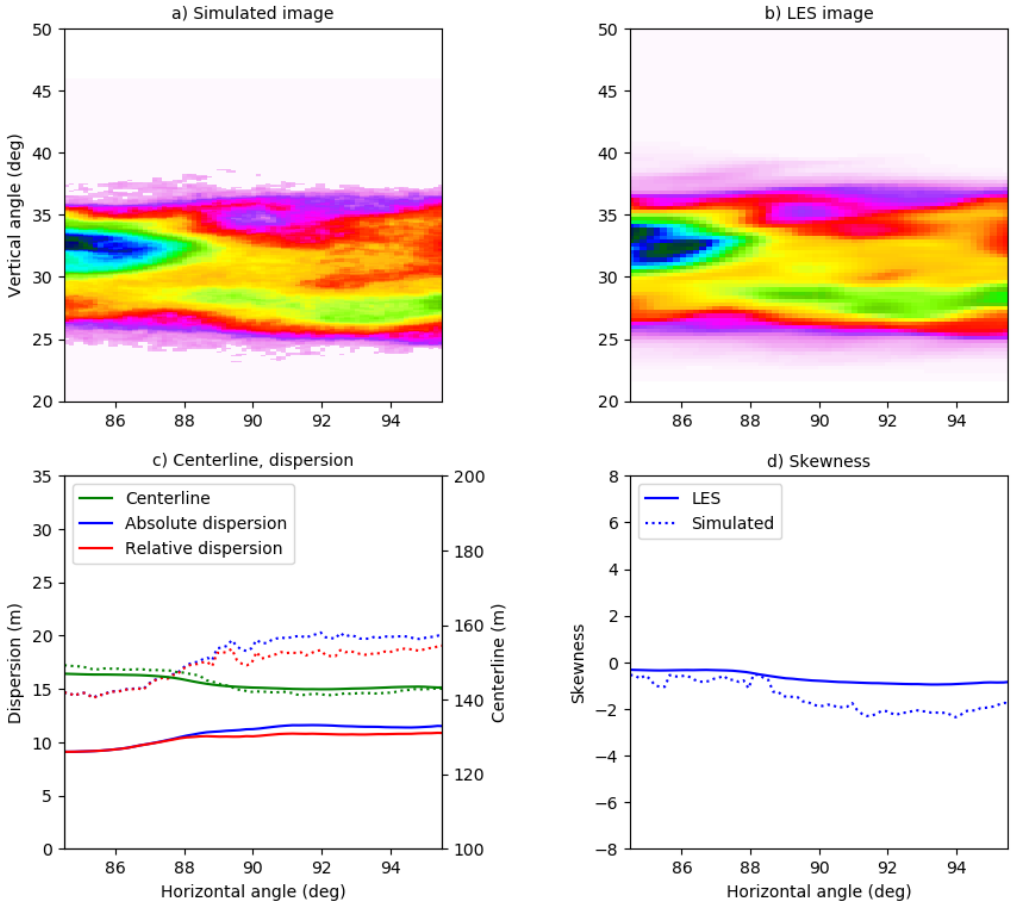

Figure 7. Similar to Fig. 4, but for camera D and time step 91.

Table 2. The mean±the standard deviation for the difference between the simulated images and the LES densities for seven (camera A) and nine (cameras B, C and D) randomly chosen time steps.

Camera	Timestep(s)	Centerline (m)	Absolute dispersion (m)	Relative dispersion (m)	Skewness
A	5, 13, 22, 31, 41, 60, 97	0.060±0.203	0.955±0.655	1.243±0.602	-0.029±0.094
B	7, 23, 32, 48, 60, 61, 65, 75 91	-0.503±1.164	-1.088±1.612	-0.240±0.565	-0.187±0.252
C	7, 23, 32, 48, 60, 61, 65, 75 91	-1.069±2.582	4.989±2.141	4.429±2.030	-0.159±0.794
D	7, 23, 32, 48, 60, 61, 65, 75 91	-0.353±2.851	7.658±1.839	7.036±1.681	0.505±1.375

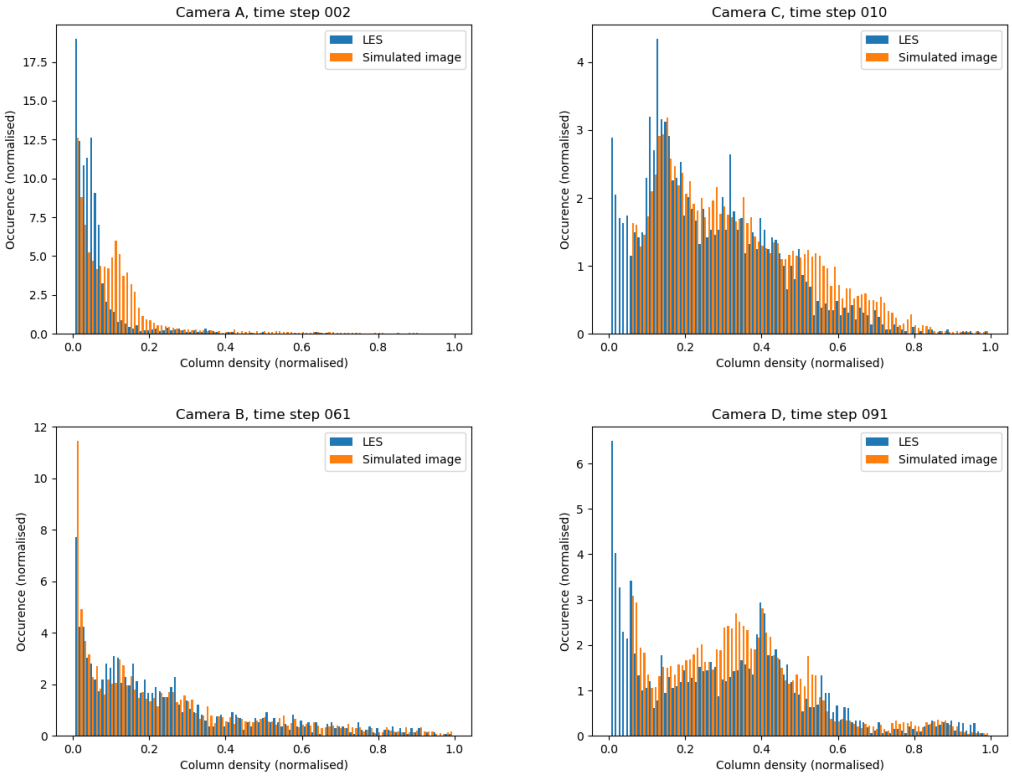

Figure 8. The probability density function (pdf) of the column densities from the LES and simulated images in Figs. 4-7.

the centerline and the dispersions the differences are about or smaller than the voxel resolution of the LES simulations. For camera C the centerline differences are about the LES voxel resolution, whereas the dispersion differences increase. Camera D differences shows similar behaviour, but with even larger differences for the dispersions. As already mentioned above, the main source for the differences is the Monte Carlo noise in the radiative transfer simulation when the SO_2 signal becomes weak. This alters the dispersions, Figs. 4-7 and pdfs, Fig. 8. This is evident in the simulated images dispersions, which are not as smooth as those from the LES, Figs. 5-.7. It must also be emphasized that the densities simulated by the LES and the apparent absorbance are not the same physical quantities, but are non-linearly connected through the radiative transfer equation.

3.2 Solar azimuth and zenith angle effects

In Figs. 3 and 4 results were shown for solar azimuth and zenith angles of $\phi_0 = 90°$ and $\theta_0 = 40°$, respectively. The simulations were repeated for a solar zenith angle of $\theta_0 = 60°$ to see if this would change the plume statistics. The difference in apparent absorbance, $\delta\tau = \tau(\theta_0 = 60) - \tau(\theta_0 = 40)$, is shown in Fig. 9. The apparent absorbance is generally slightly smaller (on average about 6%) for $\theta_0 = 60°$ than for $\theta_0 = 40°$. Ideally the apparent absorbance is due to photons travelling along a straight

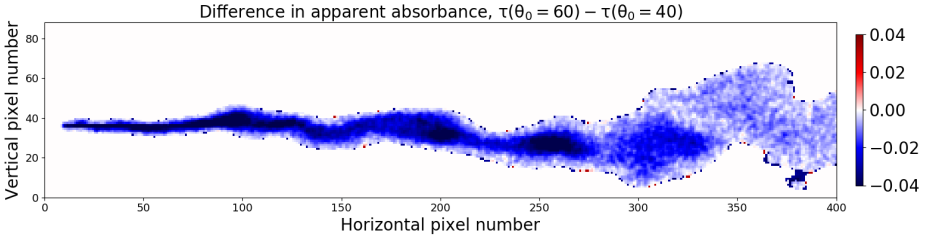

Figure 9. The difference in apparent absorbance from images recorded at two different solar zenith angles, $\theta_0 = 60^\circ$ and $\theta_0 = 40^\circ$.

lines passing through the plume and into the camera. However, photons taking other paths may also contribute to the signal. Direct solar radiation photons contribute in three ways to the camera signal through: 1) direct photons scattered behind the plume in the direction of the camera; 2) direct photons scattered in the plume towards the camera; and 3) direct photons scattered between the plume and the camera in the direction of the camera. The first part is included in the apparent absorbance and does not depend on solar zenith angle due to the background correction. The third part is called light dilution and does not depend on the amount of SO_2 in the plume. The second part depends on the amount of SO_2 in the plume and the solar zenith angle. The latter because there is relatively more direct radiation at $\theta_0 = 40^\circ$ than at $\theta_0 = 60^\circ$. Hence, more direct radiation is likely to enter the plume for $\theta_0 = 40^\circ$ and being scattered into the camera from inside the SO_2 plume. This explains the negative difference in the apparent absorbance between $\theta_0 = 60^\circ$ and $\theta_0 = 40^\circ$. It is noted that in an experimental setting, where calibrations are carried out throughout the day, solar zenith angle variations will not neccessarily give a change in SO_2.

Statistics were calculated as for the $\theta_0 = 40^\circ$ case and differences to this case are summarized in Table 3, rows labeled "$\theta_0 = 60^\circ$". In the table, differences are reported as the maximum difference in units of meters. Differences are reported both without and with the off-band correction, Eqs. 1 and 2 respectively, to quantify the impact of the correction. Overall, the statistics for the $\theta_0 = 60^\circ$ results deviate little from the $\theta_0 = 40^\circ$ case. The difference in meandering, not shown in Table 3, is negligible for this and all sensitivity cases below, and is not further discussed.

The sensitivity to the solar azimuth angle was investigated by setting the solar azimuth angle to $\phi_0 = 0, 45, 135, 180$, and 270°, while keeping the solar zenith angle at $\theta_0 = 40^\circ$. The difference in absorbance is less than 0.05% on average. The impact on the centerline, absolute and relative dispersions and skewness is negligible, see rows labeled "$\phi_0 = 0 - 270^\circ$" in Table 3. From the results no preferable solar azimuth-camera viewing direction geometry may be identified. However, note that the azimuth angle of the background image needs to be the same as for the image with SO_2. It is noted that including aerosols has negligible effect on the solar azimuth angle sensitivity, see section 3.3.

Table 3. Summary of differences in statistics between the baseline case shown in Fig. 4 and the sensitivity tests (first column). The second column reports the mean and standard deviation (std) of the difference in absorbance ($\delta\tau$). For the centerline, absolute dispersion and relative dispersion, the mean and standard deviation (std) are given in units of meters. For the azimuth dependence sensitivity, tests were made for a range of angles, the numbers in the table are the extreme values for all these tests.

Sensitivity test	$\delta\tau$ Mean±std	Centerline Mean±std	Absolute dispersion Mean±std	Relative dispersion Mean±std	Skewness Mean±std
Including off-band correction, Eq.2.					
$\theta_0 = 60^\circ$	-0.0097±0.0130	-0.0071±0.0830	0.0150±0.0740	0.0211±0.0773	-0.0125± 0.0738
$\phi_0 = 0 - 270^\circ$	-0.0005±0.0033	-0.0042±0.0498	-0.0064±0.0900	-0.0086±0.0746	-0.0055± 0.0513
BG aerosol	-0.0044±0.0089	0.0071±0.0791	-0.0066±0.0565	-0.0111±0.0665	0.0036± 0.0574
$\tau_{plume} \sim 0.5$, SSA=0.8	-0.0003±0.0025	0.0002±0.0412	-0.0036±0.0477	-0.0028±0.0387	-0.0012± 0.0274
$\tau_{plume} \sim 0.5$, SSA=1.0	-0.0003±0.0024	0.0034±0.0451	-0.0032±0.0517	-0.0025±0.0431	0.0007± 0.0312
$\tau_{plume} \sim 5.0$, SSA=0.8	-0.0035±0.0127	0.0722±1.1557	0.0023±0.0602	-0.0021±0.0473	0.2753± 4.9222
$\tau_{plume} \sim 5.0$, SSA=1.0	-0.0028±0.0088	0.0177±0.0431	-0.0055±0.0468	-0.0059±0.0402	-0.0009± 0.0391
A(0.0)-A(0.1)	-0.0013±0.0045	0.0007±0.0097	-0.0038±0.0299	-0.0048±0.0300	0.0012± 0.0320
A(1.0)-A(0.1)	0.0060±0.0172	0.0029±0.0170	0.0294±0.0359	0.0392±0.0386	-0.0031± 0.0356
Not including off-band correction, Eq.1.					
$\theta_0 = 60^\circ$	-0.0098±0.0129	-0.0074±0.0718	0.0196±0.0787	0.0242±0.0703	-0.0059± 0.0516
$\phi_0 = 0 - 270^\circ$	-0.0011±0.0028	0.0053±0.0495	-0.0094±0.1743	-0.0113±0.1669	0.0031± 0.0401
BG aerosol	-0.0045±0.0089	0.0057±0.0503	-0.0011±0.0391	-0.0045±0.0469	0.0014± 0.0354
$\tau_{plume} \sim 0.5$, SSA=0.8	0.0021±0.0033	-0.0559±1.1549	-0.0061±0.0334	-0.0053±0.0323	-0.2562± 4.9253
$\tau_{plume} \sim 0.5$, SSA=1.0	0.0012±0.0024	-0.0516±1.1553	-0.0080±0.0645	-0.0084±0.0572	-0.2568± 4.9252
$\tau_{plume} \sim 5.0$, SSA=0.8	0.0199±0.0263	-0.0317±1.1579	-0.0461±0.1675	-0.0569±0.1710	-0.2487± 4.9269
$\tau_{plume} \sim 5.0$, SSA=1.0	0.0109±0.0139	-0.0261±1.1577	-0.0253±0.0709	-0.0322±0.0767	-0.2467± 4.9267
A(0.0)-A(0.1)	-0.0013±0.0043	-0.0002±0.0079	-0.0039±0.0288	-0.0051±0.0284	-0.0001± 0.0289
A(1.0)-A(0.1)	0.0057±0.0171	0.0022±0.0168	0.0301±0.0445	0.0419±0.0432	-0.0121± 0.0466

3.3 Aerosol effects

No aerosols were included in the simulations above. Background aerosols may be present in both the plume and in the surrounding atmosphere. Furthermore, aerosol may be present in the plume due to formation of sulfate aerosol from SO_2. Both cases are investigated below.

First, background aerosol with an optical depth $t_{BG}(310) = 0.5$ and a single scattering albedo (SSA) of about 0.95 at 310 nm, were included in simulations for $\theta_0 = 40°$ (The aerosol_default option of uvspec was used, see Emde et al., 2016). The difference between the simulation including background aerosol and the aerosol free simulation is shown in Fig. 10a. Including background aerosol gives generally a slightly lower apparent absorbance, on average about 2.5% whether the off-

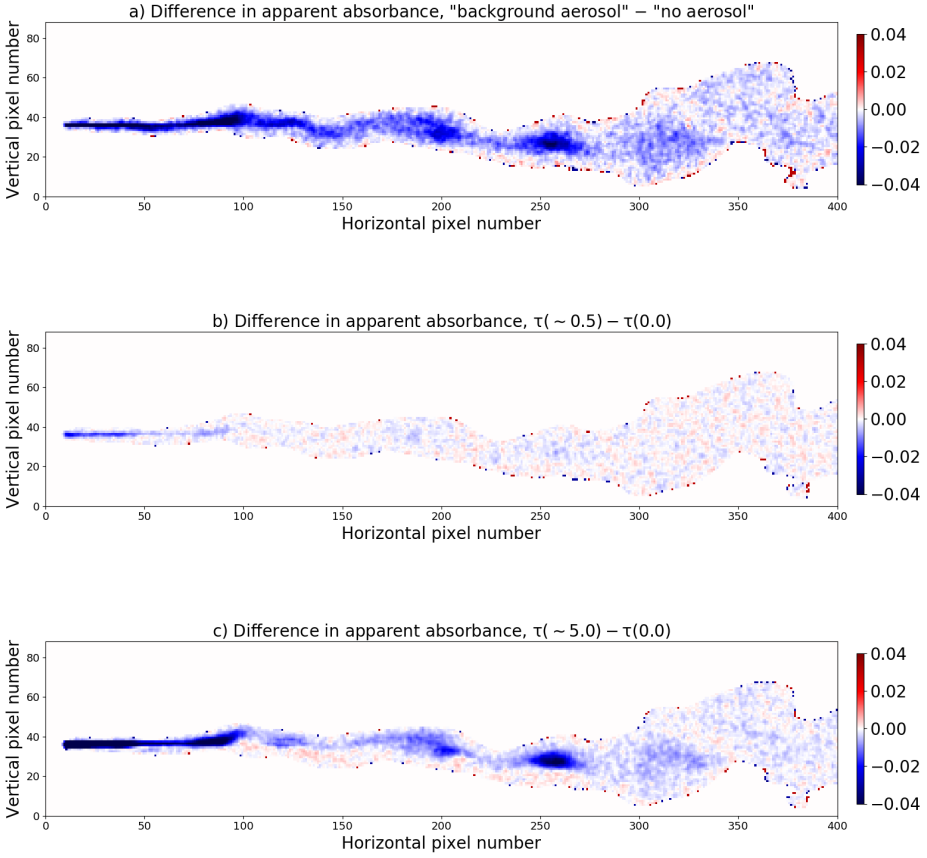

Figure 10. The difference in apparent absorbance from images recorded (a) with and without background aerosols in the atmosphere; (b-c) with and without aerosol in the plume (b): $\tau_{plume} \sim 0.5$; (c): $\tau_{plume} \sim 5.0$.

band correction is excluded or included, Eqs. 1 and 2 respectively. The decrease is due to multiple scattering by the aerosol

and hence less direct radiation (Kern et al., 2010a). The background aerosol had negligible effect on plume statistics, Table 3, rows labeled "BG aerosol".

Simulations were also made with aerosol in the plume only, that is various amounts of aerosol were added to the voxels containing SO_2. This is relevant for non-pure SO_2 plumes where aerosols are co-emitted such as from power plants, or where secondary sulfate aerosols may form in the SO_2 plume. The impact of both highly absorbing (SSA=0.8) and purely scattering aerosol (SSA=1.0) were investigated. Kern et al. (2013) concluded that if a plume contains an absorbing aerosol component the retrieved SO_2 columns may be underestimated. Here we estimate the effect of aerosols in the plume on the higher order statistics of the plume. Figs. 10b and 10c show the difference in apparent absorbance between simulations with and without absorbing aerosol in the plume for a relatively large aerosol optical depth of about 0.5 (Fig. 10b) and an unrealistic extreme case with aerosol optical depth of about 5.0 at 310 nm (Fig. 10c). Results for non-absorbing aerosol are similar (not shown).

For the more realistic value, $\tau_{plume} \sim 0.5$, Fig. 10b, there is little impact on the apparent absorbance. For (non-)absorbing aerosol with SSA=0.8 (SSA=1.0) the decrease is less than 0.2% (0.16%) on average with off-band correction, and the increase is less than 1.1% (0.63%) on average without off-band correction. For (unrealistically) large amounts of (non-)absorbing aerosol in the plume, $\tau_{plume} \sim 5.0$, the apparent absorbance decreases by less than 2% (1.5%) on average if off-band correction is included, Eq. 2. Without off-band correction, Eq. 1, the apparent absorbance increases by 9.5% (5.43%) on average. For all cases, the off-band correction reduces the influence of aerosol, as intended. For both aerosol in plume cases and whether the off-band correction was included or not, the plume statistics were affected to a negligible extent, as reported in rows labeled "τ_{plume}" in Table 3. However, the standard deviation of the skewness increase largely when aerosol influence are not corrected for, or if the plume is thick and absorbing.

The sensitivity of the solar azimuth angle when including aerosols was investigated by performing additional simulations for $\phi_0 = 45$ and 180° for the aerosol in the plume and background aerosol cases with $\tau_{plume} \sim 0.5$. The solar azimuth angle sensitivity for these cases were of the same magnitude as for the aerosol free simulations and thus of negligible impact.

3.4 Surface albedo

All simulations above were made with a surface albedo $A = 0.0$ to avoid coupling between the various processes that affect the camera images. For the wavelengths considered here the albedo for snow-free surfaces is generally small ($A < 0.1$, see for example Wendisch et al., 2004). To test the sensitivity to snow free surface albedo, simulations were made for surface albedos of $A = 0.05$ and $A = 0.1$. In addition a simulation was made with $A = 1.0$ to estimate the effect of fresh snow which has a an albedo close to one at UV wavelengths (Wiscombe and Warren, 1980). The background images were calculated for each individual case. The apparent absorbance difference for the A(0.0)-A(0.1) and A(1.0)-A(0.1) cases are shown in Fig. 11. The overall results are summarized in Table 3. Decreasing the albedo from 0.1 to 0.0 gives an overall reduction in the apparent absorbance (mostly blue colors in Fig. 11a). Compared to the $A = 0.1$ case , the $A = 0.05$ case, not shown, is about a factor of 2 smaller in magnitude for the mean apparent absorbance. Increasing the albedo from 0.1 to 1.0 gives an increase in the apparent absorbance (mostly red colors in Fig. 11b). As mentioned above, section 3.2, the apparent absorbance is due to photons travelling along straight lines passing through the plume and into the camera. However, photons scattered

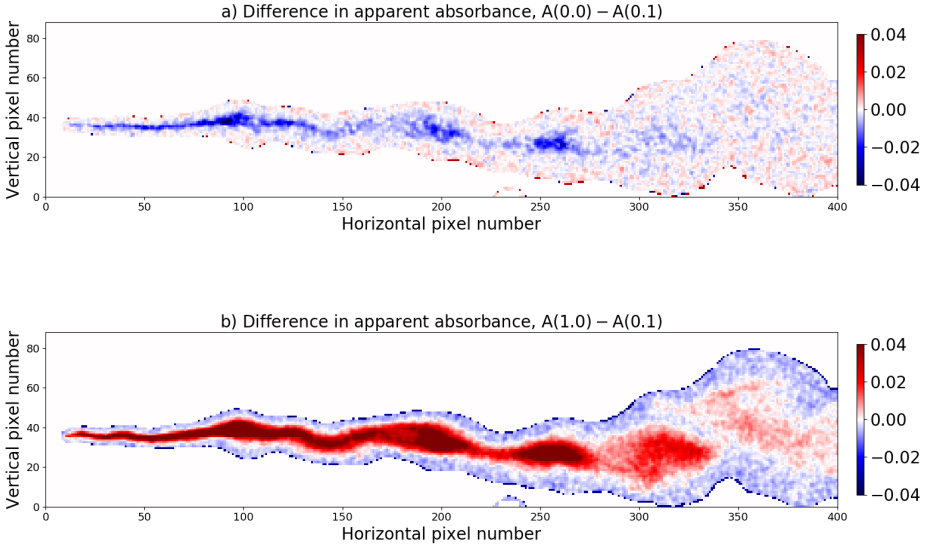

Figure 11. The difference in apparent absorbance from images recorded with surface albedo of (a) A(0.0) and A(0.1) and (b) A(1.0) and A(0.1).

between the plume and the camera, and multiple scattered photons within the plume, termed the light dilution and multiple scattering effect, respectively, may distort the apparent absorbance (Kern et al., 2012). An additional distortion, not discussed by Kern et al. (2012), is due to the surface albedo which gives additional photon paths that may contribute to the camera signal. Some photons may scatter off the surface into the plume and in the direction of the camera. This will give increased (decreased) apparent absorbance with increasing (decreasing) albedo for relatively large SO_2 concentration, see red (blue) signal in Fig. 11b (a). For small SO_2 concentrations, the light dilution effect prevails, giving a reduction (increase) in the apparent absorbance for increasing (decreasing) albedo, see blue (red) signal in Fig. 11b (a). While albedo changes may both increase and decrease the apparent absorbance, the impact on plume statistics is minor. Thus, overall, the surface albedo has negligible effect on the plume statistics (Table 3).

4 Conclusions

One novel method to measure atmospheric turbulent tracer dispersion is to use UV cameras sensitive to absorption of sunlight by SO_2. In this paper we have presented a method to simulate such UV camera measurement with a 3D Monte Carlo radiative transfer model. Input to the radiative transfer simulations are large eddy simulations (LES) of a SO_2 plume. From the simulated images various plume density statistics (centerline position, meandering, absolute and relative dispersions, skewness) were calculated and compared with similar quantities directly from the LES. Mean differences between the simulated images

and the LES were generally found to be smaller or about the size of the voxel resolution of the LES for the centerline. For the higher order statistics the differences increase as the SO_2 absorption gets weaker for a more and more dispersed plume.

Furthermore sensitivity studies were made to quantify how changes in solar azimuth and zenith angles, aerosol (background and in plume), and surface albedo, impact the UV camera image plume statistics. It was found that changing the parameters describing these effects within realistic limits, had negligible effect on the centerline position, meandering, absolute and relative dispersions, and skewness of the SO_2 plume.

Based on the simulated UV camera images and the comparison with the LES, it can be concluded that UV camera images of SO_2 plumes may be used to derive plume statistics of relevance for the study of atmospheric turbulence.

Code availability. The libRadtran software used for the radiative transfer simulations is available from www.libradtran.org. The PALM model system was used for the LES and it is available from palm.muk.uni-hannover.de/trac.

Author contributions. AK performed the radiative transfer simulations. HA, MC and SYP were responsible for the LES. AK prepared the manuscript with contributions from all co-authors.

Competing interests. The authors declare that no competing interests are present.

Acknowledgements. The Comtessa project has received funding from the European Research Council (ERC) under the European Union's Horizon 2020 research and innovation programme under grant agreement no. 670462. The resources for the numerical simulations and data storage were provided by UNINETT Sigma2 - the National Infrastructure for High Performance Computing and Data Storage in Norway under projects NN9419K and NS9419K. The reviewers' comments greatly helped improve the manuscript and we thank them for this.

References

Anderson, G., Clough, S., Kneizys, F., Chetwynd, J., and Shettle, E.: AFGL atmospheric constituent profiles (0-120 km), *Tech. Rep. AFGL-TR-86-0110*, Air Force Geophys. Lab., Hanscom Air Force Base, Bedford, Mass., 1986.

Ardeshiri, H., Cassiani, M., Park, S., Stohl, A., I.Pisso, and Dinger, A.: On the convergence and capability of large eddy simulation for passive plumes concentration fluctuations in an infinite-Re neutral boundary layer, Boundary-Layer Meteorol., accepted for publication, 2020.

Brown, R. J. and Bilger, R. W.: An experimental study of a reactive plume in grid turbulence, Journal of Fluid Mechanics, 312, 373–407, https://doi.org/10.1017/S0022112096002054, 1996.

Buras, R. and Mayer, B.: Efficient unbiased variance reduction techniques for Monte Carlo simulations of radiative transfer in cloudy atmospheres: The solution, J. Quant. Spectrosc. Radiat. Transfer, 112, 434–447, doi:10.1016/j.jqsrt.2010.10.005, 2011.

Cassiani, M., Stohl, A., and Eckhardt, S.: The dispersion characteristics of air pollution from the world's megacities, Atmospheric Chemistry and Physics, 13, 9975–9996, https://doi.org/10.5194/acp-13-9975-2013, https://www.atmos-chem-phys.net/13/9975/2013/, 2013.

Celik, I., Klein, M., and Janicka, J.: Assessment measures for engineering les application, J. Fluid Eng, 131(3), 031 102, 2009.

Deardorff, J.: The use of subgrid transport equations in a three-dimensional model of atmospheric turbulence, J. Fluid Eng, 95, 429–438, 1973.

Dinger, A. S., Stebel, K., Cassiani, M., Ardeshiri, H., Bernardo, C., Kylling, A., Park, S.-Y., Pisso, I., Schmidbauer, N., Wasseng, J., and Stohl, A.: Observation of turbulent dispersion of artificially released SO_2 puffs with UV cameras, Atmospheric Measurement Techniques, 11, 6169–6188, https://doi.org/10.5194/amt-11-6169-2018, https://www.atmos-meas-tech.net/11/6169/2018/, 2018.

Dosio, A. and de Arellano, J. V.-G.: Statistics of Absolute and Relative Dispersion in the Atmospheric Convective Boundary Layer: A Large-Eddy Simulation Study, Journal of the Atmospheric Sciences, 63, 1253–1272, https://doi.org/10.1175/JAS3689.1, http://dx.doi.org/10.1175/JAS3689.1, 2006.

Emde, C., Buras, R., Mayer, B., and Blumthaler, M.: The impact of aerosols on polarized sky radiance: model development, validation, and applications, Atmos. Chem. Phys., 10, 383–396, http://www.atmos-chem-phys.net/10/383/2010/, 2010.

Emde, C., Buras-Schnell, R., Kylling, A., Mayer, B., Gasteiger, J., Hamann, U., Kylling, J., Richter, B., Pause, C., Dowling, T., and Bugliaro, L.: The libRadtran software package for radiative transfer calculations (version 2.0.1), Geoscientific Model Development, 9, 1647–1672, https://doi.org/10.5194/gmd-9-1647-2016, http://www.geosci-model-dev.net/9/1647/2016/, 2016.

Fossum, H. E., Reif, B. A. P., Tutkun, M., and Gjesdal, T.: On the Use of Computational Fluid Dynamics to Investigate Aerosol Dispersion in an Industrial Environment: A Case Study, Boundary-Layer Meteorology, 144, 21–40, https://doi.org/10.1007/s10546-012-9711-z, https://doi.org/10.1007/s10546-012-9711-z, 2012.

Gant, S. and Kelsey, A.: Accounting for the effect of concentration fluctuations on toxic load for gaseous releases of carbon dioxide, Journal of Loss Prevention in the Process Industries, 25, 52 – 59, https://doi.org/https://doi.org/10.1016/j.jlp.2011.06.028, http://www.sciencedirect.com/science/article/pii/S0950423011001094, 2012.

Gliß, J., Stebel, K., Kylling, A., and Sudbø, A.: Improved optical flow velocity analysis in SO_2 camera images of volcanic plumes – implications for emission-rate retrievals investigated at Mt Etna, Italy and Guallatiri, Chile, Atmospheric Measurement Techniques, 11, 781–801, https://doi.org/10.5194/amt-11-781-2018, https://www.atmos-meas-tech.net/11/781/2018/, 2018.

Hermans, C., Vandaele, A., and Fally, S.: Fourier transform measurements of SO_2 absorption cross sections:: I. Temperature dependence in the 24 000-29 000 cm^{-1} (345-420 nm) region, Journal of Quantitative Spectroscopy and Radiative Transfer, 110, 756–765,

https://doi.org/http://dx.doi.org/10.1016/j.jqsrt.2009.01.031, http://www.sciencedirect.com/science/article/pii/S0022407309000375, {HITRAN}, 2009.

Hilderman, T., Hrudey, S., and Wilson, D.: A model for effective toxic load from fluctuating gas concentrations, Journal of Hazardous Materials, 64, 115 – 134, https://doi.org/https://doi.org/10.1016/S0304-3894(98)00247-7, http://www.sciencedirect.com/science/article/pii/S0304389498002477, 1999.

Kern, C., Deutschmann, T., Vogel, L., Wöhrbach, M., Wagner, T., and Platt, U.: Radiative transfer corrections for accurate spectroscopic measurements of volcanic gas emissions, Bull Volcanol, 72, 233–247, 2010a.

Kern, C., Kick, F., Lübcke, P., Vogel, L., Wöhrbach, M., and Platt, U.: Theoretical description of functionality, applications, and limitations of SO_2 cameras for the remote sensing of volcanic plumes, Atmospheric Measurement Techniques, 3, 733–749, https://doi.org/10.5194/amt-3-733-2010, http://www.atmos-meas-tech.net/3/733/2010/, 2010b.

Kern, C., Deutschmann, T., Werner, C., Sutton, A. J., Elias, T., and Kelly, P. J.: Improving the accuracy of SO2 column densities and emission rates obtained from upward-looking UV-spectroscopic measurements of volcanic plumes by taking realistic radiative transfer into account, Journal of Geophysical Research: Atmospheres, 117, https://doi.org/10.1029/2012JD017936, http://dx.doi.org/10.1029/2012JD017936, 2012.

Kern, C., Werner, C., Elias, T., Sutton, A. J., and Lübcke, P.: Applying UV cameras for SO2 detection to distant or optically thick volcanic plumes, Journal of Volcanology and Geothermal Research, 262, 80–89, https://doi.org/http://dx.doi.org/10.1016/j.jvolgeores.2013.06.009, http://www.sciencedirect.com/science/article/pii/S0377027313001832, 2013.

Kylling, A., Buras, R., Eckhardt, S., Emde, C., Mayer, B., and Stohl, A.: Simulation of SEVIRI infrared channels: a case study from the Eyjafjallajökull April/May 2010 eruption, Atmospheric Measurement Techniques, 6, 649–660, https://doi.org/10.5194/amt-6-649-2013, http://www.atmos-meas-tech.net/6/649/2013/, 2013.

Lateb, M., Meroney, R., Yataghene, M., Fellouah, H., Saleh, F., and Boufadel, M.: On the use of numerical modelling for near-field pollutant dispersion in urban environments - A review, Environmental Pollution, 208, 271–283, https://doi.org/https://doi.org/10.1016/j.envpol.2015.07.039, http://www.sciencedirect.com/science/article/pii/S0269749115003723, special Issue: Urban Health and Wellbeing, 2016.

Lübcke, P., Bobrowski, N., Illing, S., Kern, C., Alvarez Nieves, J. M., Vogel, L., Zielcke, J., Delgado Granados, H., and Platt, U.: On the absolute calibration of SO_2 cameras, Atmospheric Measurement Techniques, 6, 677–696, https://doi.org/10.5194/amt-6-677-2013, http://www.atmos-meas-tech.net/6/677/2013/, 2013.

Maronga, B., Gryschka, M., Heinze, R., Hoffmann, F., Kanani-Sühring, F., Keck, M., Ketelsen, K., Letzel, M. O., Sühring, M., and Raasch, S.: The Parallelized Large-Eddy Simulation Model (PALM) version 4.0 for atmospheric and oceanic flows: model formulation, recent developments, and future perspectives, Geoscientific Model Development, 8, 2515–2551, https://doi.org/10.5194/gmd-8-2515-2015, https://www.geosci-model-dev.net/8/2515/2015/, 2015.

Mayer, B. and Kylling, A.: Technical note: the libRadtran software package for radiative transfer calculations-description and examples of use, Atmos. Chem. Phys., 5, 1855–1877, 2005.

Mayer, B., Hoch, S. W., and Whiteman, C. D.: Validating the MYSTIC three-dimensional radiative transfer model with observations from the complex topography of Arizona's Meteor Crater, Atmos. Chem. Phys., 10, 8685–8696, 2010.

Moeng, C.: A large-eddy simulation model for the study of planetary boundary-layer turbulence, J. Atmos. Sci, 41, 2052–2062, 1984.

Mori, T. and Burton, M.: The SO2 camera: A simple, fast and cheap method for ground-based imaging of SO2 in volcanic plumes, Geophysical Research Letters, 33, https://doi.org/10.1029/2006GL027916, https://agupubs.onlinelibrary.wiley.com/doi/abs/10.1029/2006GL027916, 2006.

Pope, S. B.: Turbulent Flows, Cambridge University Press, 2000.

Raasch, S. and Schröter, M.: PALM A large-eddy simulation model performing on massively parallel computers, Meteorologische Zeitschrift, 10, 363–372, https://doi.org/doi:10.1127/0941-2948/2001/0010-0363, https://www.ingentaconnect.com/content/schweiz/mz/2001/00000010/00000005/art00001, 2001.

Schauberger, G., Piringer, M., Schmitzer, R., Kamp, M., Sowa, A., Koch, R., Eckhof, W., Grimm, E., Kypke, J., and Hartung, E.: Concept to assess the human perception of odour by estimating short-time peak concentrations from one-hour mean values. Reply to a comment by Janicke etÂ al., Atmospheric Environment, 54, 624 – 628, https://doi.org/https://doi.org/10.1016/j.atmosenv.2012.02.017, http://www.sciencedirect.com/science/article/pii/S135223101200132X, 2012.

Stull, R. B.: An Introduction to Boundary Layer Meteorology, Kluwer Academic Publishers, Boca Raton, 1988.

Vilà-Guerau de Arellano, J., Dosio, A., Vinuesa, J.-F., Holtslag, A. A. M., and Galmarini, S.: The dispersion of chemically reactive species in the atmospheric boundary layer, Meteorology and Atmospheric Physics, 87, 23–38, https://doi.org/10.1007/s00703-003-0059-2, https://doi.org/10.1007/s00703-003-0059-2, 2004.

Wendisch, M., Pilewskie, P., Jäkel, E., Schmidt, S., Pommier, J., Howard, S., Jonsson, H. H., Guan, H., Schröder, M., and Mayer, B.: Airborne measurements of areal spectral surface albedo over different sea and land surfaces, J. Geophys. Res., 109, D08 203, doi:10.1029/2003JD004 393, 2004.

Wiscombe, W. J. and Warren, S. G.: A model for the spectral albedo of snow, I, Pure snow, J. Atmos. Sci., 37, 2712–2733, 1980.